MRS Communications (2019), 1 of 9

doi:10.1557/mrc.2019.113

MRS Communications

Research Letter

Variations in electronic states of coumarin hexanethiolate-labeled i-Au_{25} and bi-Au_{25} clusters

Angela Meola†, Nicole Hondrogiannis†, and **Pierce Brown,** Department of Chemistry, Towson University, Towson, MD 21252, USA
Maksym Zhukovskyi, Department of Chemistry and Biochemistry, University of Notre Dame, Notre Dame, IN 46556, USA
Zheng Zheng and **Zeev Rosenzweig,** Department of Chemistry and Biochemistry, University of Maryland Baltimore County, Baltimore, MD 21250, USA
Keith Reber and **Mary Sajini Devadas,** Department of Chemistry, Towson University, Towson, MD 21252, USA
Address all correspondence to Mary Sajini Devadas at **mdevadas@towson.edu**

(Received 20 June 2019; accepted 8 August 2019)

Abstract

$Au_{25}(C_6H_{14}S)_{18}^-$ icosahedron and $[Au_{25}(PPh)_{10}(C_6H_{14}S)_5Cl_2]^{2+}$ bi-icosahedron clusters were synthesized. Ligand exchange reactions were carried out with a new coumarin-derived fluorophore (Cou-SH) to label both clusters. Labeled and unlabeled Au_{25} were compared and the changes in the electronic structure were determined. The labeled clusters showed marked changes in electronic states, as evidenced by the quenching in the UV region and enhancement in the near infrared. The quantum yield from Cou-SH decreased and the quantum yield from the labeled Au_{25} increased. Second, the authors observed changes in the electrochemical band gap.

Introduction

The electronic and optical properties of gold nanoparticles are integral in developing the technology for electronic warfare platforms for the obscuration and attenuation of light, medical detection technology for the treatment of cancer, nanoparticle sensors, and high-resolution biological imaging.[1–3] Variations in the nanoparticle size, stabilizing ligand, and geometry can influence the electrochemical potential, quantum yield, and nonlinear optical properties. The absorbance spectra of gold nanoparticles that display quantum confinement, electronic transitions between the ligand and the gold core in the higher frequency regions of the electromagnetic spectrum are observed.[4–6] The lower frequency transitions that are associated with the gold–gold interactions are seen in the near infrared (NIR) region.[1,7] The crystal structures of icosahedral and bi-icosahedral structures have generated an interest in the last decade. This is because, in the bi-structure, the majority of the Au atoms form the core as opposed to the shell. The icosoheral Au_{25} contains 13 core atoms, whereas the latter contains a dimer of 13 Au atoms, connected by a single vertex Au atom while retaining the same Au–Au distance. Both clusters also show a structured spectral profile analogous to molecules.[8,9] It is of general interest to compare the optical properties of these crystals (i- and bi-) with and without fluorophore labeling. This is because the quasicontinuous electronic bands in large nanoparticles (>5 nm) evolve to discrete levels as the size decreases to 1.3 nm and below. This leads to superatom behavior.[10,11] Typically, the ligand's role in these clusters is to prevent the aggregation of the metal core and therefore has negligible contribution to the energetics of the gold cluster. We believe that the careful choice of ligands could influence the core states. A few studies investigate the influence of chromophore on the electronic energy levels of the Au core or shell atomic orbitals.[12–15] There are a few groups that have investigated the direct approach of synthesizing these clusters with fluorophores. Kamat and coworkers[13,14] have shown increased quantum yield in plasmonic nanoparticles (>2 nm) made with pyrene, as a result of electron transfer from the chromophore to the gold nanoparticle. Lee and coworkers[16] have shown a directional electron transfer from i-Au_{25} to a modified pyrene. The closed shell arrangement of the icosahedron and bi-icosohedral crystal lattice geometries produces the possibility of superatom properties if a potential is generated by tuning the surface of the cluster.[17–19] The energy barrier between a chromophore ligand and the gold core creates a potential for quantum tunneling. Fluorophores bound to nanocrystals display increased luminescence and photostability that apply to super high-resolution imaging when attached to the nanoparticle surface.[20,21] This can be extended to applications such as solar energy storage and conversion if the electron localization/delocalization can be determined.[22]

The literature suggests that electronic transfers between the ligand and gold core are possible as opposed to the naturally occurring fundamental process of excitation energy transfer involving an electronic transfer from a donor to an

† These authors contributed equally to this work.

accepter.[16,19,23] Forster resonance energy transfer explains the energy transfer exchange between two fluorescent species.[3] The fluorescence and electrochemical properties of the gold cluster can be affected when coupled to a chromophore. As this can alter the optical properties such as an increase or a decrease in the quantum yield by the changes in the electronic states due to the possibility of electron density transfer from the ligand to the gold cluster or vice versa. Previously, Murray and coworkers[24] and Pineda and coworkers[25] have shown the possibility of multi-electron transfer (even if the redox processes were quasi-reversible) that the rate of electron transfer is dependent on the composition of the protecting layers and not on the core metal.

In this paper, we compare the properties of two well-defined crystal structures of the magic numbered cluster Au_{25} with and without fluorophore labeling the iscosohedral $Au_{25}(C_6H_{14}S)_{18}^-$ (i-Au_{25}) and $[Au_{25}(PPh)_{10}(C_6H_{14}S)\ Cl_2]^{2+}$ (bi-Au_{25}). Ligand exchange reactions were performed with the coumarin hexanethiol ligand (Cou-SH), with the aim of labeling the cluster and at a minimal loading of 1 Cou-SH per cluster on an average. A coumarin-based ligand was chosen because coumarins are a naturally occurring versatile class of compounds that are under extensive study in use as an anticancer drug design. They are widely used and synthesized for pharmaceutical and homeopathic therapies. Coumarin are used as anticoagulants, antispasmodic agents, antioxidants, hepatoprotective, anti-inflammatory, antiviral, and antifungal, and they have offered benefits to people with coronary disease.[26] A recent research, involving the anticancer properties of coumarin subclasses, has shown positive results in the cytotoxicty of cancer cells during in vitro studies.[26,27] This is the first study with the ligand (Cou-SH). The ligand-exchanged products with the Cou-SH will be referred to as i-Au_{25}LE and bi-Au_{25}LE. In this paper, we present a comparative study of the i- and bi-products. The motivation for the study comes from the possibility of the particle's potential facilitating directional transitions of electrons and a ligand enhanced optical response in gold nanoclusters, as described by Fortunelli and coworkers.[5] Below, we present (i) the successful synthesis of the labeled clusters and their size distribution through a high-resolution transmission electron microscopy, (ii) the optical properties through UV–vis absorption, steady-state fluorescence, and IR spectroscopies, and (iii) electrochemical properties through square-wave voltammetry to investigate ground-state electron transfer.

Materials and methods

Chemicals for synthesis

The materials supplied by the manufacturers were Sigma Aldrich: gold(III) chloride ($HAuCl_4$ reagent grade), sodium borohydride ($NaBH_4$, 99%), tetraoctylammonium bromide (TOABr, 98%), toluene (C_7H_8 reagent grade, 99.5%); Fisher Chemical: NaOH (98%), methanol (CH_3OH HPLC-grade), acetone (C_3H_6O ACS-grade); Acros Organics: hexanethiol ($C_6H_{14}S$ 96%), dichloromethane ($CH_2Cl_2$98%); and Milli-Q water purified using a Millipore Milli-Q system (18.2 MΩ·cm)

One-pot synthesis of $Au_{25}(C_6H_{13}S)_{18}$ or i-Au_{25}

A modified literature procedure was used.[28] The reaction was conducted at room temperature in air. In a 250-mL round bottom flask, 2.5 mM (0.7854 g) of tetraoctylammonium bromide (TOABr) was dissolved in 50 mL of methanol with a magnetic stirring at a medium speed. Dissolved 0.9 mM (0.3 g) of gold (III) chloride trihydrate ($HAuCl_4$) in the TOABr solution is continuously stirred. The solution was stirred for no longer than 15 min before the color changed from yellow to a deep red. 4.8 mmol (820 µL) of hexanethiol was added to the solution. The solution became colorless within 15 min. Once the solution became colorless, it could be stirred for 30 min. 13.7 mmol (0.52 g) of $NaBH_4$ was dissolved in 5 mL of Milli-Q water at pH 10 and was chilled to 0 °C. The mixture was added all at once to the gold solution. Hydrogen gas evolved, and the solution immediately turned dark brown and the clusters precipitated out. The solution was then allowed to stir for 24 h. After the 24-h duration, we decanted the solution and the product into a centrifuge tube and centrifuged for 5 min at 3900 rpm. Then, the methanol solvent was decanted and discarded and 10 mL of methanol was added to the centrifuge tube, and the tube was shaken to disperse the product. This was then centrifuged for another 5 min at 3900 rpm, decanted and the solution was discarded unless the product dissolved (if the product began to dissolve then it was decanted, retained, and the methanol rinse was repeated until the solution was clear). A 10 mL aliquot of acetone was added to the centrifuge tube and shaken gently to disperse. Again, centrifugation was carried out for 5 min at 3900 rpm and the acetone extract was decanted into a scintillation vial. The acetone solution contained i-Au_{25}. The steps were repeated of re-extracting with 10 mL acetone aliquots and centrifuging until the solution was clear. This indicated that all the i-Au_{25} has been extracted. The product was then rotary evaporated, re-extracted with 3 mL aliquots of acetone until clear, and syringe filtered with a 0.45-µm Teflon filter. Once the extraction of i-Au_{25} was complete, a liquid–liquid extraction was performed. A 1:1:1 ratio of i-Au_{25} product, Milli-Q water, and toluene was added to a clean centrifuge tube and vigorously shaken to mix the solvents, the excess polymer formed a white precipitate almost immediately. The mixture was centrifuged at 2000 rpm for 5 min. The white polymer layer was discarded. The golden layer was separated from the brown layer into two 250 mL round bottom flasks. All extracted samples were then rotary evaporated and washed with methanol for 1 h to remove the excess ligand. The average yield of $Au_{25}(C_6H_{13}S)_{18}$ was 15–20%.

Synthesis of $[Au_{25}(PPh)_{10}(C_6H_{14}S)_5Cl_2]^{2+}$ or bi-Au_{25}

An organic one-phase method was conducted under ambient conditions at room temperature and standard atmosphere. 0.25 mmol of Au PPh_3Cl in 20 mL of a 3:1 dichloromethane/ethanol ratio was dissolved and stirred for 30 min at room temperature. Using a transfer pipette, 74 µL (0.50 mmol) of

https://doi.org/10.1557/mrc.2019.113

hexanethiol was added. The solution was allowed to stir at a moderate speed for 30 min (the solution remained clear during these steps). To chilled 5 mL of Milli-Q water to approximately 0 °C, 0.1800 g of $NaBH_4$ (2.5 mmol) was added. Immediately, the $NaBH_4$ was decanted into the solution and the stirring speed was increased (the solution began to turn gold to dark brown immediately). The solution was allowed to stir for 3 h then decanted into a separatory funnel. 10 mL aliquots of Milli-Q were added into the funnel and inverted several times. Then, the product was allowed to separate from the Milli-Q and removed. This step was repeated three more times to remove the excess $NaBH_4$. The product was dried with sodium sulfate, then a Hirsch funnel was used with a filter paper and the drying agent was separated. The product was washed with the filter paper using 10 mL aliquots of methanol. The product was rotary evaporated before washing with 10 mL aliquots of hexane and ethyl acetate for 1 h continuously. After washing and removing larger particles, the bi-Au_{25} was extracted with 5 mL aliquots of methanol. The average yield was 10%.

Synthesis of i-Au_{25}LE

16.9 mg of $Au_{25}(C_6H_{13}S)_{18}$ and 0.4 mg of the Cou-SH ligand were dissolved in 10 mL of dichloromethane and allowed to stir for 1 h. The solution was then rotary evaporated. The product was washed with 10 mL of methanol three times at 1-h intervals and then used for characterization.

Synthesis of bi-Au_{25}LE

18.4 mg of $[Au_{25}(PPh)_{10}(C_6H_{14}S)_5Cl_2]^{2+}$ and 0.4 mg of Cou-SH ligand were dissolved in 10 mL of dichloromethane and allowed to stir for 48 h. The solution was then rotary evaporated. The product was washed with 10 mL of hexane three times at 1-h intervals.

Synthesis of Cou-SH

The detailed synthesis and characterization of the new coumarin hexanethiolate ligand is given in the Supplementary Material.

UV–vis absorbance measurements

UV–vis absorbance measurements were collected n the 200–1100 nm range and used to examine the ground-state absorption and charge transfers. An Agilent Technologies Cary 60 instrument was used for particle characterization, dye quantification, the determination of optical density prior to fluorescence measurements, and the calculation of extinction coefficient measurements. UV–vis characterization methods involved the identification of documented absorption peaks for each material by recording the electronic spectra of solutions that have absorbance <1 as required by Beer-Lambert's Law. Fluorophore quantification procedures involved a baseline subtraction of the particle synthesized with hexanethiol. Each dye exchange product was measured for the relative quantifiable enhancement at 320 nm due to the Cou-SH ligand. The dye quantification process involved a series of procedures where the extinction coefficient for the gold particles was measured at the peak center at 680 nm associated with the sp ← sp transition, and the coumarin ligand extinction coefficient was calculated at 320 nm. The absorption from the gold on the exchange product was calculated and subtracted from the total absorbance at 320 nm. The calculation steps are given in Supplementary Material.

IR measurements

IR measurements were recorded using Thermo Scientific Nicolet iS10. The gold cluster solutions and Cou-SH were dissolved in dichloromethane (Acros Organics). A drop of the sample was added on to the ATR plate and allowed to dry before the spectrum was recorded in each case.

Proton NMR

Proton NMR data for each exchange product and the coumarin ligand were collected on a JEOL 400 SS 400 MHz instrument using a deuterated chloroform containing TMS standard. Gold exchange products were sonicated for 5 min in deuterated chloroform with iodine crystals to break the gold bonds. The proton NMR spectra were collected for the coumarin-derived ligand that was used for the exchange synthesis and compared to identify all peaks present in the scan. The integration ratio of a known single unique hydrogen atom on both the hexanethiol and coumarin hexanethiol ligand was used to identify the number of coumarin dyes on each exchange product. The ratio was compared to the results determined through absorption subtraction with UV–vis spectrophotometry.

Steady-state fluorescence

Steady-state fluorescence measurements were collected on a Horiba Jobin Yvon FluoroMax-4 spectrofluorometer and used to calculate the quantum yield in the ultraviolet and NIR regions. Emission spectra were collected with an excitation wavelength at 320 nm and 3-by-3 slit width to measure luminescence in the range 340–600 nm. The NIR luminescence for i-Au_{25} was collected with a 680 nm excitation wavelength, 5-by-5 slit width, and ranged from 690 to 900 nm. The NIR luminescence measurements of the bi-Au_{25} products were collected with a 670 nm excitation wavelength, 5-by-5 slit width, and ranged from 690 to 900 nm. The particles synthesized with hexanethiol were also characterized through fluorescence emission spectra. A stock solution of each particle was prepared with optical density at approximately 0.1 a.u. at $\lambda = 320$ nm. The samples were measured in triplicate using 2 mL aliquots of stock solution for each measurement. The average of all three spectra was graphed for each region. In addition, the average integration value and and the standard deviation were calculated. Quantum yield measurements for all particles were calculated at 320 nm with reference to Bis-MSB for the UV region. Phthalocyanine was used as a reference for quantum yield calculations in the NIR region. To calculate the quantum yield for the UV–vis and NIR regions, the integration value of each spectra is compared to the reference spectra and the

https://doi.org/10.1557/mrc.2019.113

absorbance ratio. The ratio of the solvent refractive index is also considered.

Fluorescence lifetime measurements

Fluorescence lifetime measurements were performed on a PTI-Horiba QuantaMaster 400 with a PicoMaster TCSPC steady-state fluorescence lifetime spectrometer. A 375 nm femtosecond pulsed laser diode, operated at 1 MHz, was the excitation source for all particle fluorescence lifetime measurements. The analysis of all lifetime traces was completed using the PTI-Horiba Felix-GX software.

Transmission electron microscopic images

Transmission electron microscopic (TEM) images were collected on a JEOL 2011, TEM 80–200 kV, 0.14 nm resolution. The images were utilized to determine the purity and size distribution. The average core diameter was determined using the Image J software. The average particle diameter and standard deviation were calculated based on a sample size of 100 or more measurements. Histograms were plotted to indicate a Gaussian distribution for particle size.

Electrochemical measurements

Electrochemical measurements were collected on a CH instrument 620D hardware station equipped with leads for a trielectrode system. Electrochemical potential was measured for each particle using a self-constructed silver quasi-reversible electrode. The trielectrode was assembled for the working, reference, and counter electrode. The working and counter electrodes each contained a 2 cm platinum wire soldered to the end of a copper wire. The reference electrode was soldered to a 2 cm silver wire. A protective shrink casing was applied with a heat gun before the assembled wires were placed in a plastic mold. A viscous solution of 5.128 g of poly(bisphenol A-co-epichlorohydrin) glycidyl end-capped and 0.734 g of *m*-phenylenediamine was made into a solution by heating. The solution was poured into the plastic mold and allowed to sit at room temperature for 15 min before being placed in the oven at 80 °C for 24 h. Square-wave voltametry (SWV) measurements were taken in a dichloromethane solvent containing 0.1 M Bu_4NClO_4 as the supporting electrolyte. Fisherbrand No. 37 white septa were used with 10 mL glass vials and parafilmed to degas the samples with argon. They were degassed for 30 min at room temperature before being placed in an isopropanol and dry ice mixture. The sample was purged for another 10 min and chilled to −78 °C (this was done only for the i-Au_{25}). The band gap from the first oxidation peak to the reduction peak was measured.

Results and discussion

Monodispersed particles of both crystal structures (i- and bi-) were synthesized and characterized before and after ligand exchange reactions. Size dispersity was confirmed through TEM images that resulted in a Gaussian particle distribution. The particle diameters were 1.15 ± 0.30, 1.17 ± 0.27, 0.90 ± 0.16, and 0.87 ± 0.17 nm for i-Au_{25}, i-Au LE, bi-Au_{25}, and bi-Au_{25}LE, respectively. Representative TEM micrographs and their corresponding size distribution histograms are shown in Figs. 1(a)–1(h). This supports the fact that the size of the original clusters did not change after the ligand exchange reactions in both crystal systems and is supported by the UV–vis optical absorbance spectra, as seen in Figs. 2(a) and 2(b). The spectra indicate the characteristic molecule-like transitions as expected for i-Au_{25} at 1.8, 2.7, 3.1, and 3.8 eV and at 1.9, 2.8, 2.9, 3.3, 3.7, and 3.9 eV for bi-Au_{25}, respectively. It should be noted that the 3.9 eV transition in Cou-SH overlaps with the molecular transition of Au_{25} indicated by the change in the doublet-like peak to a single peak in the UV spectra of the ligand-exchanged products in the 3.9 eV region. The overlaid spectra indicate slight energy shifts when the Cou-SH is bound to the gold cluster, indicating the formation of a covalent bond between Cou-SH and the nanoparticle (Supplementary Fig. S1). The presence of the key transitions at 1.8 eV (sp ← sp)[29] for i-Au_{25}LE and at 1.9 eV for the bi-Au_{25}LE is an indication that the size of the clusters did not change after the exchange reaction was performed. This is attributed to the contributions solely from the atomic orbitals of the 13 core gold atoms. For bi-Au_{25}LE, this transition is slightly higher which can be attributed to additional electron transfer capabilities of the triphenylphosphine ligand.[29]

Steady-state fluorescence indicated quenching in the UV–vis region from the naked Cou-SH when bound to the surface of gold cluster. Figures 2(c)–2(f) give the visible and NIR emission profiles of i-Au_{25}, i-Au_{25}LE, bi-Au_{25}, and bi-Au_{25}LE, respectively. The visible luminescence of the Cou-SH has an emission maxima of 383 nm. This peak is quenched and red-shifted in the product to 403 nm in i-Au_{25}LE (Supplementary Fig. S1(c)). In addition, the quantum yield (Φ) changes from $0.0377 \pm 1.2 \times 10^{-4}$ to $0.000257 \pm 6.8 \times 10^{-4}$ in i-Au_{25}LE. In the bi-system, the Cou-SH peak did not show a peak shift and remains at 383 nm (Fig. 2 and Supplementary Fig. S1 (d)). This supports the fact that the Cou-SH is replaced in the bridging location of the thiol ligands and bound to the bridging staples. However, there was a decrease in the quantum yield to $0.011 \pm 2.8 \times 10^{-4}$ from $0.0377 \pm 1.2 \times 10^{-4}$ in the NIR region.

The NIR emission peak was observed at 803 nm in the i-Au_{25} product and 828 nm in the bi-Au_{25} product. In the exchanged products i-Au_{25}LE and bi-Au_{25}LE, there is a blue shift in the emission maxima to 768 and 825 nm, respectively, and peak broadening (Fig. 2 and Supplementary Fig. S1(e) and (f)). This indicates that the incoming ligand Cou-SH is affecting the mixed ligand outer shell and is interacting with the core atomic orbitals. This is further supported by the quenching of fluorescence in the visible region with a Stokes shift for Cou-SH and further proved spectroscopically with the other techniques such as IR spectroscopy and HNMR later. We project that the Cou-SH is located on the staple motif in the case of the i-structure and the bridging location in the case of bi-Au_{25}. In addition to the blue shift in the spectra, there was also an enhancement in quantum yield from the unexchanged i-Au_{25}

https://doi.org/10.1557/mrc.2019.113

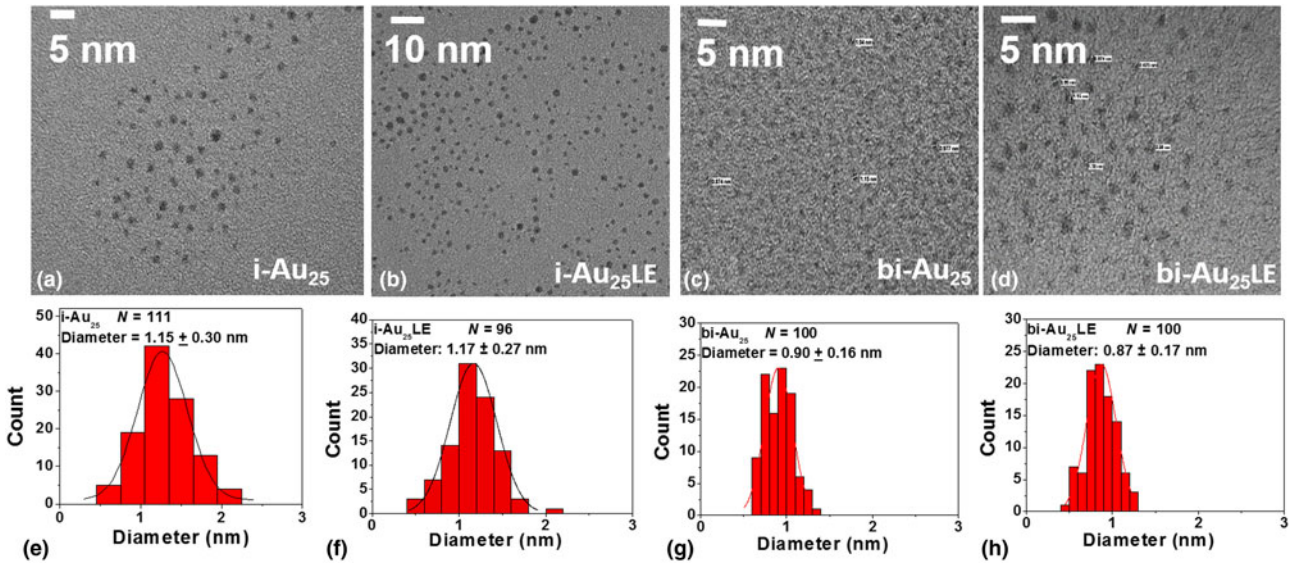

Figure 1. TEM analysis of the i-Au_{25}, i-Au_{25}LE, bi-Au_{25}, and bi-Au_{25}LE. (a)–(d) Micrographs of the i- and bi-products with and without Cou-SH and (e)–(h) the size distribution histograms.

($\Phi = 0.000929$) and bi- Au_{25} ($\Phi = 0.003180$) to the ligand-exchanged products $\Phi = 0.00026$ and $\Phi = 0.003677$ for i-Au_{25}LE and bi-Au_{25}LE, respectively (Figs. 2(e) and 2(f)). Time-correlated single-photon counting measurements were done on the labeled and unlabeled or unexchanged structures. However, due to the lifetimes being faster than the instrument response factor/resolution, we have shown for qualitative purposes the change in the exponential decay for the exchanged product as opposed to the free dye in Supplementary Figs. S2 (a) and S2(b) and their lifetimes in Supplementary Table S1. Additionally, IR spectroscopy was performed on the products to prove that there was no free Cou-SH in either system. This is indicated by the absence of the S–H vibrational stretch at 2556 cm^{-1} in both i-Au_{25}LE and bi-Au_{25}LE. The comparative spectra are given in Figs. 2(g) and 2(h).

Figure 3 gives the proton NMR spectra of the ligand-exchanged products. Regions of interest were chosen in each case. The peak integral values for the methoxy group of Cou-SH (3.85 ppm) and the $–CH_2$ on the α-carbon (2.7 ppm) on hexanethiol were used to find the number of dyes per cluster in i-Au_{25}LE. Similarly, for bi-Au_{25}LE, the same groups were chosen in addition to the α- and α′-carbon on the triphenylphosphine groups (7.4 ppm). The dye quantification with UV–vis subtraction and proton NMR resulted in a similar whole number formula of 1 and 3 on an average per particle for i-Au_{25}LE and bi-Au_{25}LE, respectively. The integration values are given in Supplementary Table S2.

Electrochemical measurements were pursued to determine changes in the bandgap. The shift of the open circuit potential from zero indicated that the particles were a charged species. The square wave voltammograms (SWVs) of i-Au_{25} and bi-Au_{25} clusters corresponded with previously documented findings.[30] The variation in the electrochemical gap between the two core structures is indicative of the structural differences. The ligand-exchanged SWVs suggest an electron transfer reaction in both cases instead of mass transfer as the UV spectra before and after the electrochemical measurements did not show significant changes. The i-Au_{25} systems were taken at −75 °C. The band gap changed from 1.76 to 1.64 V and in the bi-Au_{25} system, measured at room temperature the band gap changed from 1.4 to 1.2 V. The electrochemical bandgap measurements obtained from the SWV of bi-Au_{25} with that of the i-Au_{25} cluster were compared to reveal the electronic energy structure near the HOMO−LUMO levels. Lee and coworkers[7] have shown that the band gap is smaller for the rod-shaped bi-Au_{25} compared to i-Au_{25}. The decrease in the band gap in i-Au_{25}LE to 1.64 V and in bi-Au_{25}LE cluster to 1.2 V suggest significant electronic variations owing to replacement of the hexanethiol ligand with the Cou-SH in the staple motif S–Au–S–Au–S. Wang and coworkers[31] have reported previously that strong coupling exists between the Au core and ligand energy states with durene–dithiolate ligands. They noted that the electrochemical energy gap of bi-Au_{25} is also substantially smaller (1.4 V, measured at room temperature) than that of an icosahedral Au_{13} cluster (1.76 V) that was assigned as $Au_{13}(PPh_3)_4(SC_{12}H_{25})_2Cl_2$ by Menard et al..[24] In Fig. 4, the peak at +0.6 V is the oxidation potential from the internal standard ferrocence and not from the ligand. The peak at −1.8 V is due to Cou-SH. Pineda and coworkers[25] have also shown that the substituents on the $Au_{25}L_{18}$ clusters, where L = hexanethiol, have a direct effect on the redox potentials favoring reduction rather than oxidation. In addition, they have demonstrated that there are changes in bandgap only when there are electron donating or withdrawing groups, and this

https://doi.org/10.1557/mrc.2019.113

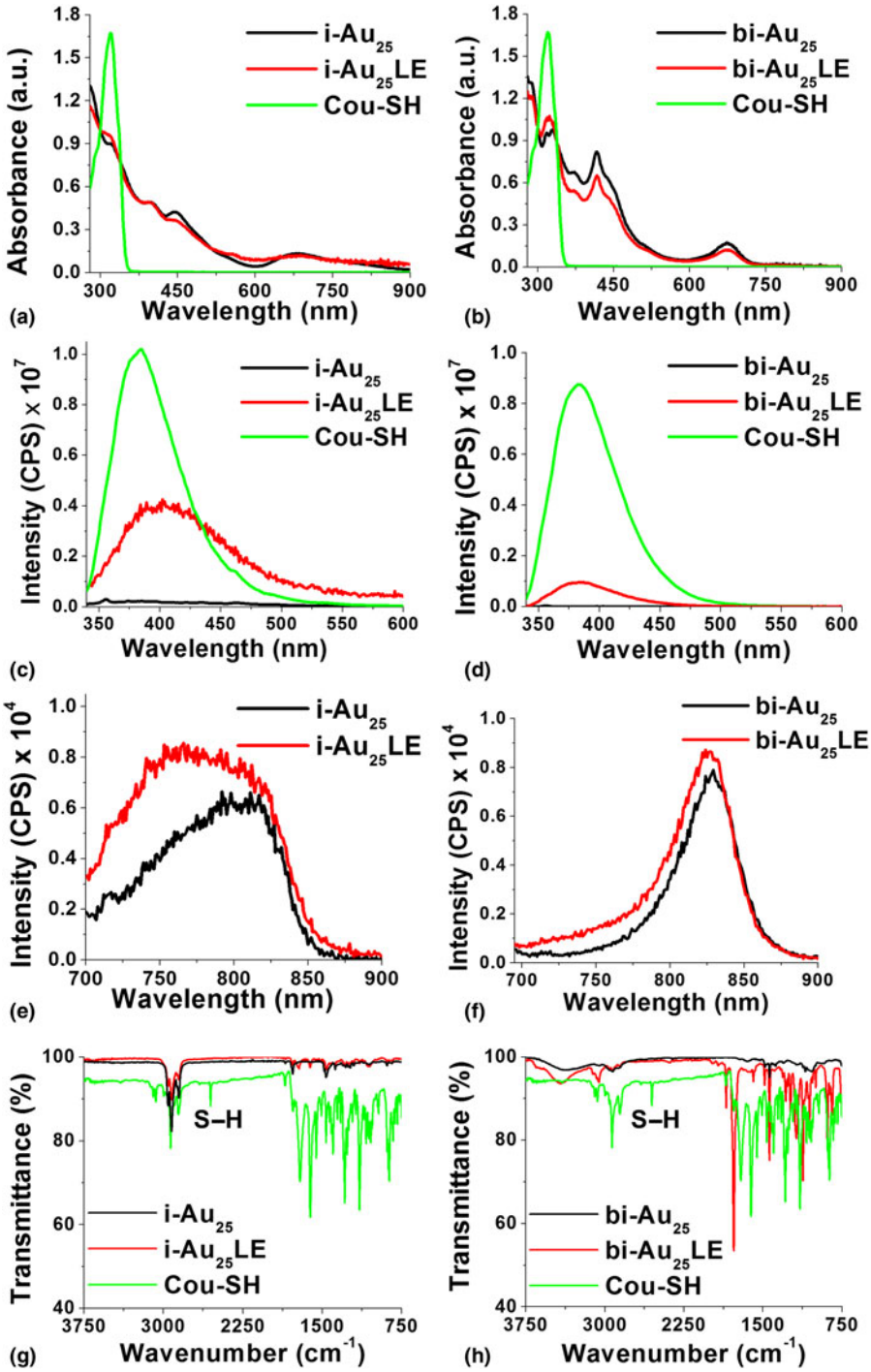

Figure 2. Comparison of the absorption, emission, and IR spectra of the i-Au_{25} and bi-Au_{25} before and after ligand exchange. (a) and (b) UV–vis spectra of i-Au_{25} and bi-Au_{25}. (c) and (d) Emission spectra in the visible region of i-Au_{25} and bi-Au_{25} excited at 320 nm before and after ligand exchange. (e) and (f) Emission spectra of the same in the NIR region excited at 670 nm. (g) and (h) IR spectra of i-Au_{25} and bi-Au_{25} before and after ligand exchange, indicating the absence of the S–H stretch in the products.

could be as large as 0. 45 V. Ramakrishna and coworkers[32] have also shown that this changes could also be attributed to electrostatic field effects due to the structure of the ligand and the substituents on the aromatic ring of Cou-SH.[33]

In conclusion, we synthesized and characterized the ligand-exchanged products of i-Au_{25} and bi-Au_{25} with Cou-SH to produce i-Au_{25}LE and bi-Au_{25}LE, respectively. We compared the optical and electrochemical changes and

https://doi.org/10.1557/mrc.2019.113

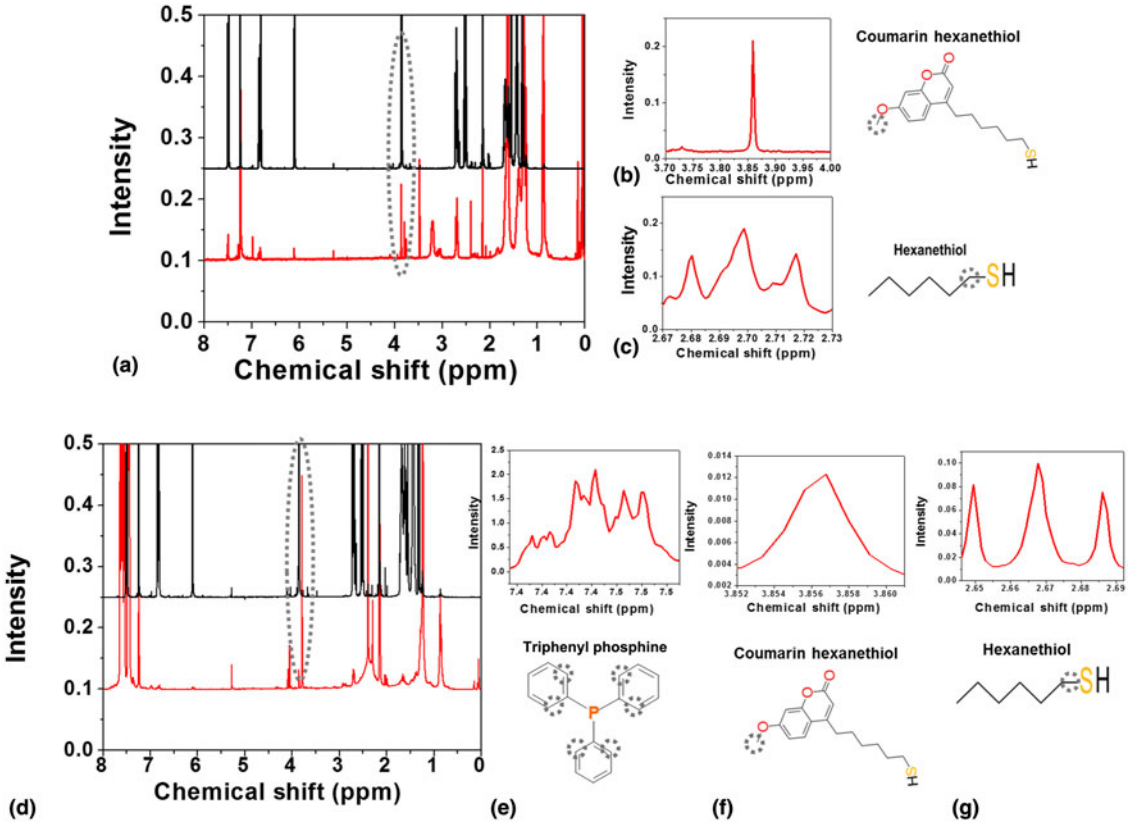

Figure 3. Comparison of proton NMR analysis: (a) proton NMR of Cou-SH and i-Au_{25}LE, the methoxy peak from the Cou-SH is circled in gray. (b) Region of interest (ROI) spectra from protons on the methoxy group and ligand structure. (c) Triplet from the protons on α-carbon from the thiol group in hexanethiol and its chemical structure. (d) Proton NMR of Cou-SH and bi-Au_{25}LE, the methoxy peak from the Cou-SH is circled in gray. (e) ROI spectra from protons on the triphenylphosphine adjacent to the phosphorus bond. (f) ROI spectra from protons on the methoxy group and ligand structure. (g) Triplet from the protons on α-carbon from the thiol group in hexanethiol and its chemical structure.

projected the location of the incoming ligand based on bandgap changes, quenching of fluorescence, and the absence of S–H stretch in the IR spectra. Additionally, qualitative lifetimes indicate the attachment of Cou-SH to the cluster. In both cases, we note that the hexanethiol ligand was successfully replaced with Cou-SH. Additionally, we have shown the possibility of electron density transfer in the ground state due to changes in the bandgap, as noted from the square wave volatammograms. Fortunelli and coworkers[5] have proved by time-dependent density functional theory that aromatic ligands with tailored electron withdrawing groups exhibiting steric hindrance achieve charge decompression at the surface-enhancing light

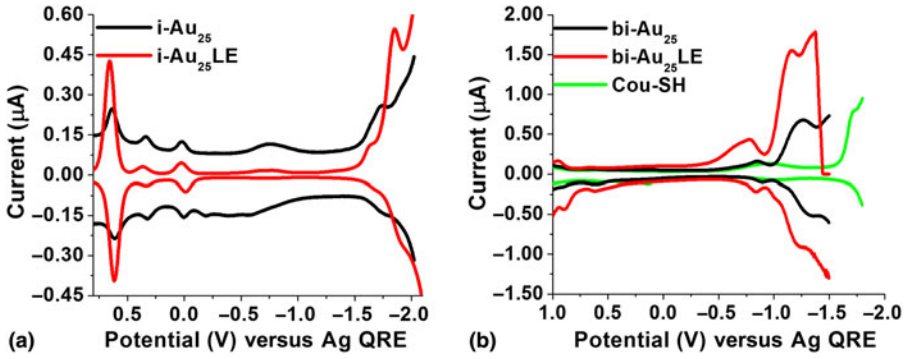

Figure 4. Comparison of the square wave voltammograms of the (a) i- and (b) bi-Au_{25} products with the unbound Cou-SH.

https://doi.org/10.1557/mrc.2019.113

absorption. This warrants additional studies of the excited state through transient absorption measurements. These clusters labeled with fluorophores can be used as excellent two-photon imaging agents and light-harvesting capabilities owing to the strong luminescence in the NIR region and the possibility to change the ligand states to fine tune the localization/delocalization of electrons.

Supplementary material

The supplementary material for this article can be found at https://doi.org/10.1557/mrc.2019.113.

Acknowledgments

We are grateful to Dr. Masaru Kuno for allowing us to use the TEM at the University of Notre Dame and ThermoFisher Corporation. We also thank Mr. Stephen Blama for his help with EDS. This work was supported by NSF MRI-1626326, and Towson University Fisher Chair, Fisher General Endowment, Faculty Development Research Committee, Fisher College Undergraduate Research, and Graduate Student Association Grants.

Conflicts of interest

The authors declare no conflicts of interest.

References

1. A.U. Sokolnikov: *THz Identification for Defense and Security Purposes: Identifying Materials, Substances, and Items* (World Scientific Publishing Company, Singapore/USA, 2013).
2. J.S. Tate, S. Espinoza, D. Habbit, C. Hanks, W. Trybula, and D. Fazarro: Military and national security implications of nanotechnology. *J. Technol. Studies* **41**, 20 (2015).
3. O. Manzoor, N. Soleja, and M. Mohsin: Nanoscale gizmos – the novel fluorescent probes for monitoring protein activity. *Biochem. Eng. J.* **133**, 83 (2018).
4. P. Angelova, N. Kuchukova, G. Dobrikov, I. Petkova, I. Timtcheva, K. Kostova, E. Vauthey, and E. Giorgetti: Design, synthesis and photophysical study of fluorophore modified noble metal nanoparticles. 2010 12th International Conference on Transparent Optical Networks, Munich, 2010, pp. 1–4. doi: 10.1109/ICTON.2010.5549256.
5. L. Sementa, G. Barcaro, O. Baseggio, M. De Vetta, A. Dass, E. Aprà, M. Stener, and A. Fortunelli: Ligand-enhanced optical response of gold nanomolecules and its fragment projection analysis: the case of Au30(SR)18. *J. Phys. Chem. C* **121**, 10832 (2017).
6. D.R. Kauffman, D. Alfonso, C. Matranga, P. Ohodnicki, X. Deng, R.C. Siva, C. Zeng, and R. Jin: Probing active site chemistry with differently charged Au25q nanoclusters (q = −1, 0, +1). *Chem. Sci.* **5**, 3151 (2014).
7. S. Park and D. Lee: Synthesis and electrochemical and spectroscopic characterization of biicosahedral Au25 clusters. *Langmuir* **28**, 7049 (2012).
8. M. Zhu, C.M. Aikens, F.J. Hollander, G.C. Schatz, and R. Jin: Correlating the crystal structure of a thiol-protected Au25 cluster and optical properties. *J. Am. Chem. Soc.* **130**, 5883 (2008).
9. Y. Shichibu, Y. Negishi, T. Watanabe, N.K. Chaki, H. Kawaguchi, and T. Tsukuda: Biicosahedral gold clusters [Au25(PPh3)10(SCnH2n+1)5Cl2]2 + (n = 2−18): a stepping stone to cluster-assembled materials. *J. Phys. Chem. C* **111**, 7845 (2007).
10. M. Walter, J. Akola, O. Lopez-Acevedo, P.D. Jadzinsky, G. Calero, C.J. Ackerson, R.L. Whetten, H. Grönbeck, and H. Häkkinen: A unified view of ligand-protected gold clusters as superatom complexes. *Proc. Natl Acad. Sci.* **105**, 9157 (2008).
11. S.N. Khanna and P. Jena: Assembling crystals from clusters. *Phys. Rev. Lett.* **69**, 1664 (1992).
12. X. Kang, H. Chong, and M. Zhu: Au25(SR)18: the captain of the great nanocluster ship. *Nanoscale* **10**, 10758 (2018).
13. K.G. Thomas and P.V. Kamat: Making gold nanoparticles glow: enhanced emission from a surface-bound fluoroprobe. *J. Am. Chem. Soc.* **122**, 2655 (2000).
14. K.G. Thomas and P.V. Kamat: Chromophore-functionalized gold nanoparticles. *Acc. Chem. Res.* **36**, 888 (2003).
15. F. Stellacci, C.A. Bauer, T. Meyer-Friedrichsen, W. Wenseleers, S.R. Marder, and J.W. Perry: Ultrabright supramolecular beacons based on the self-assembly of two-photon chromophores on metal nanoparticles. *J. Am. Chem. Soc.* **125**, 328 (2003).
16. M.S. Devadas, K. Kwak, J.-W. Park, J.-H. Choi, C.-H. Jun, E. Sinn, G. Ramakrishna, and D. Lee: Directional electron transfer in chromophore-labeled quantum-sized Au25 clusters: Au25 as an electron donor. *J. Phys. Chem. Lett.* **1**, 1497 (2010).
17. H. Qian, Y. Zhu, and R. Jin: Atomically precise gold nanocrystal molecules with surface plasmon resonance. *Proc. Natl Acad. Sci.* **109**, 696 (2012).
18. K.L.D.M. Weerawardene and C.M. Aikens: Origin of photoluminescence of Ag25(SR)18–nanoparticles: ligand and doping effect. *J. Phys. Chem. C* **122**, 2440 (2018).
19. Z. Liu, Q. Xu, S. Jin, S. Wang, G. Xu, and M. Zhu: Electron transfer reaction between Au25 nanocluster and phenothiazine-tetrachloro-p-benzoquinone complex. *Int. J. Hydrogen Energy* **38**, 16722 (2013).
20. C. Leduc, J.-M. Jung, R.R. Carney, F. Stellacci, and B. Lounis: Direct investigation of intracellular presence of gold nanoparticles via photothermal heterodyne imaging. *ACS Nano* **5**, 2587 (2011).
21. J.-Q. Goh, S. Malola, H. Häkkinen, and J. Akola: Role of the central gold atom in ligand-protected biicosahedral Au24 and Au25 clusters. *J. Phys. Chem. C* **117**, 22079 (2013).
22. M. Zhou, R. Jin, M.Y. Sfeir, Y. Chen, Y. Song, and R. Jin: Electron localization in rod-shaped triicosahedral gold nanocluster. *Proc. Natl Acad. Sci* **114**, E4697 (2017).
23. R. Banerjee, C. Maiti, S. Dutta, and D. Dhara: Size- and distance-dependent excitation energy transfer in fluorophore conjugated block copolymer – gold nanoparticle systems. *Polymer* **59**, 243 (2015).
24. L.D. Menard, S.-P. Gao, H. Xu, R.D. Twesten, A.S. Harper, Y. Song, G. Wang, A.D. Douglas, J.C. Yang, A.I. Frenkel, R.G. Nuzzo, and R.W. Murray: Sub-nanometer Au monolayer-protected clusters exhibiting molecule-like electronic behavior: quantitative high-angle annular dark-field scanning transmission electron microscopy and electrochemical characterization of clusters with precise atomic stoichiometry. *J. Phys. Chem. B* **110**, 12874 (2006).
25. D. García-Raya, R. Madueño, M. Blázquez, and T. Pineda: Electrochemistry of molecule-like Au25 nanoclusters protected by hexanethiolate. *J. Phys. Chem. C* **113**, 8756 (2009).
26. S. Emami and S. Dadashpour: Current developments of coumarin-based anti-cancer agents in medicinal chemistry. *Eur. J. Med. Chem.* **102**, 611 (2015).
27. I. Lagunes, P. Begines, A. Silva, A.R. Galán, A. Puerta, M.X. Fernandes, I. Maya, J.G. Fernández-Bolaños, Ó López, and J.M. Padrón: Selenocoumarins as new multitarget antiproliferative agents: synthesis, biological evaluation and in silico calculations. *Eur. J. Med. Chem.* **179**, 493 (2019).
28. A. Dass, A. Stevenson, G.R. Dubay, J.B. Tracy, and R.W. Murray: Nanoparticle MALDI-TOF mass spectrometry without fragmentation: Au25(SCH2CH2Ph)18 and mixed monolayer Au25(SCH2CH2Ph)18−x (L)x. *J. Am. Chem. Soc.* **130**, 5940 (2008).
29. H. Qian, W.T. Eckenhoff, M.E. Bier, T. Pintauer, and R. Jin: Crystal structures of Au2 complex and Au25 nanocluster and mechanistic insight into the conversion of polydisperse nanoparticles into monodisperse Au25 nanoclusters. *Inorg. Chem.* **50**, 10735 (2011).
30. K. Kwak, V.D. Thanthirige, K. Pyo, D. Lee, and G. Ramakrishna: Energy gap law for exciton dynamics in gold cluster molecules. *J. Phys. Chem. Lett.* **8**, 4898 (2017).
31. T. Ahuja, D. Wang, Z. Tang, D.A. Robinson, J.W. Padelford, and G. Wang: Electronic coupling between ligand and core energy states in dithiolate-monothiolate stabilized Au clusters. *Phys. Chem. Chem. Phys.* **17**, 19342 (2015).

32. M. Shabaninezhad, A. Abuhagr, N.A. Sakthivel, C. Kumara, A. Dass, K. Kwak, K. Pyo, D. Lee, and G. Ramakrishna: Ultrafast electron dynamics in thiolate-protected plasmonic gold clusters: size and ligand effect. *J. Phys. Chem. C* **123**, 13344 (2019).
33. K. Kwak and D. Lee: Electrochemical characterization of water-soluble Au25 nanoclusters enabled by phase-transfer reaction. *J. Phys. Chem. Lett.* **3**, 2476 (2012).

https://doi.org/10.1557/mrc.2019.113